Extreme shearography

Development of a high-speed shearography instrument for quantitative surface strain measurements during an impact event

Anisimov, Andrei G.; Groves, Roger M.

DOI
10.1016/j.optlaseng.2020.106502

Publication date
2021

Document Version
Final published version

Published in
Optics and Lasers in Engineering

Optics and Lasers in Engineering 140 (2021) 106502

Contents lists available at ScienceDirect

Optics and Lasers in Engineering

journal homepage: www.elsevier.com/locate/optlaseng

Extreme shearography: Development of a high-speed shearography instrument for quantitative surface strain measurements during an impact event

Andrei G. Anisimov*, Roger M. Groves

Aerospace Non-Destructive Testing Laboratory, Faculty of Aerospace Engineering, Delft University of Technology, the Netherlands

ARTICLE INFO

Keywords:
High-speed shearography
Double-pulse shearography
Flexural waves
Impact
Composite materials
Surface strain

ABSTRACT

Monitoring of extreme dynamic loadings on composite materials with high temporal and spatial resolution provides an important insight into the understanding of the material behaviour. Quantitative measurement of the surface strain at the first moments of the impact event may reveal the initiation of the failure mechanisms leading to damage. For this purpose, we developed a shearography instrument for strain measurements during a severe impact event at μs temporal resolution. This paper presents the design, development and experimental measurement of the surface strain during an impact on aluminium and composite samples. The final design realises measurements of the in- and out-of-plane surface strain components to improve coupling of experimental data with the numerical models. The experiments on aluminium and composite specimens revealed the main elastic material response to be in the first 1-2 μs after the impact followed by the initiation and propagation of flexural waves causing in- and out-of-plane deformation. Further analysis of the wavefronts will be used as input and validation data for new numerical and analytical models of the impact response of composites and for validation of other experimental techniques as acoustic emission and embedded piezo sensors.

The set of technical parameters of the developed shearography instrument makes it one of the most extreme applications of shearography for material characterisation. The framework for this work is the "EXTREME Dynamic Loading – Pushing the Boundaries of Aerospace Composite Material Structures" Horizon 2020 project.

1. Introduction

Improving the impact response of composite materials is an important direction of the materials development towards safer and lighter aircraft. Composite materials are vulnerable to extreme dynamic loadings such as blade off events or foreign object damage (hail, runway debris, bird strike) [1]. The development of new instruments to reconstruct extreme dynamic events and to measure failure parameters will provide an important insight into the understanding of the behaviour of composites. The strain development during the impact is of particular interest for both materials modelling and for experimental researchers [2,3]. The shearography (speckle pattern shearing interferometry) technique [4–6] is used in this project to provide a quantitative measurement of the surface strain development at the first moments of the impact event (μs time scale) which may reveal the initiation of the failure mechanisms in composite materials.

In practice, shearography has actively been used for non-destructive inspection or testing (NDI, NDT) of composite materials over more than 20 years [5,7,8], mostly for defect detection, localisation and characterisation. A posterior inspection of impact damage has been reported in the literature for both low [9–11] and high-velocity impacts [12]. Shearography has also already been used for the experimental mechanics of composites at slow strain rates [5,13–15], but not during an impact event at high impact speeds and energies. Previously holographic techniques were used to capture the propagation of flexural waves during the impact force with classical (film) pulsed holography [16,17] and later with the electronic speckle pattern interferometry (ESPI) by introducing a carrier frequency [18]. Double pulse ESPI has been actively used for impact monitoring [19,20] and numerical comparison with the available finite element models [21,22].

When shearography is used for the monitoring of dynamic events, the phase corresponding to the surface displacement gradient of the object can be extracted from captured interferograms without time-averaging by using a spatial phase-shift and Fourier-based processing [23]. The first spatial phase-shift for shearography used a carrier spatial frequency generated by a Mach-Zehnder interferometer [24]. Recently, various configurations of spatial phase-shift with a Mach-Zehnder interferometer were developed [25,26] and later the Michelson interferometer was

* Corresponding author at: Kluyverweg 1, 2629 HS, Delft, the Netherlands
E-mail address: a.g.anisimov@tudelft.nl (A.G. Anisimov).

https://doi.org/10.1016/j.optlaseng.2020.106502
Received 4 July 2020; Received in revised form 11 October 2020; Accepted 23 November 2020

also adapted for this purpose [27] and improved by using a slit instead of a circular aperture to improve the energy efficiency and quality of the revealed phase maps [28]. Alternative methods were also reported with a camera coupled with an array of micro-polarisers [29], a dual-wavelength method with a synthetic wavelength [30] and with diffractive optical elements [31].

Dynamic loading with a high speed of deformation requires the highest possible acquisition rate, reaching μs and sub-μs temporal resolution. Various solutions for fast shearography have been reported which employed high-speed [32] or more often double frame cameras with a higher spatial resolution [33]. The double frame approach was also used for vibration analysis in a frequency range up to a few kHz [34–36], including for transient vibrations [37,38] and impact-induced flexural waves at low impact energies [39,40]. Most of the reported shearography instruments with spatial phase-shift implemented out-of-plane deformation analysis with the shear applied in one direction per experiment due to the complexity of the optical parts and phase extraction. However, there were recent results with the shear simultaneously applied in both x- and y-directions by multiplexing using polarisation [41,42], different spectral ranges [43] and spatial phase-shifting [44].

This paper presents the final results of the development and experimental testing of the new high-speed EXTREME shearography instrument, which was performed in two configurations with a modified Michelson and double imaging Mach-Zehnder interferometers, respectively [45,46]. Both configurations are presented and compared when used for high-speed shearography. The latter one was used for the final design as it allows an independent adjustment of the shear amount. The development was driven by the need to maximise the value of the expected results for the validation of numerical models – to measure both in- and out-of-plane surface strain components at impact speeds up to 200 m/s with μs temporal resolution over the field of view around 100×100 mm. Therefore two viewing directions (shearing interferometers) with a double-frame approach were used to capture the interferograms during the impact. The main results include experimentally measured surface strain maps over the field of view during impact events on aluminium and composite samples.

The framework for this work is the "EXTREME Dynamic Loading – Pushing the Boundaries of Aerospace Composite Material Structures" Horizon 2020 project [47]. Within the project, the shearography data is fused with high-speed 3D digital image correlation (DIC) [48] and in-situ impact data from fibre optical sensors based on Fibre Bragg Gratings (FBG), embedded and surface mounted piezo-electric sensors [49].

2. High-speed shearography theory

Shearography is a coherent-optical technique that realises full-field direct measurement of the surface displacement gradient when the object is deformed. In this project, the object is deformed by impact loading with a gas-gun using an impactor. As in the literature [33–36], a pulsed laser is used here to produce a speckle pattern by illuminating the object with an expanded laser beam. Interferograms are recorded with cameras through shearing devices at the initial moment of the impact (from 0 to 10 μs after the impact). During the impact event, each camera records interferograms synchronously with the laser pulses and realises spatial phase-shifting to give the shearography phase corresponding to the surface displacement gradient which was built up in between laser pulses. This phase map is further processed under certain design considerations, e.g. cameras and lasers orientation, to give the surface strain components.

In general, to measure the in- and out-of-plane surface strain components, a multicomponent 3D shearography configuration is needed, e.g. with three shearing cameras [5]. Due to the expected complexity of the high-speed shearography instrument [45,46], the number of shearing cameras was reduced to two with the main sensitivity to the in- and out-of-plane components. A schematic of the EXTREME shearography instrument is presented in Fig. 1.

When two shearing cameras are used, each of them will provide a phase change $\Delta\phi_x$ which can be extracted from the Fourier side-spectra of the recorded interferograms [25]. If the illumination and viewing directions are in the xz-plane and a relatively small shear distance d_x is applied in the x-direction (the shear is significantly smaller than the distance to the object), the phase change $\Delta\phi_x$ becomes a function of the in- and out-of-plane surface strain components ($\partial u/\partial x$ and $\partial w/\partial x$, respectively):

$$\Delta\phi_x = \phi_x^{'} - \phi_x^{ref} = \frac{2\pi}{\lambda}\left(k_x\partial u/\partial x + k_y\partial v/\partial x + k_z\partial w/\partial x\right)d_x \overset{\text{if in } xz \text{ plane}}{\approx} \frac{2\pi}{\lambda}\left(k_x\partial u/\partial x + k_z\partial w/\partial x\right)d_x, \quad (1)$$

where ϕ_x' and ϕ_x^{ref} are the signal and reference phase differences obtained before and after deformation, subscript x refers to the shear direction, λ is the laser wavelength, and $(k_x\ k_y\ k_z)$ are components of the sensitivity vector, that is the bisector of the viewing angle Θ between the illumination and viewing directions [5]. The surface strain components $\partial u/\partial x$ and $\partial w/\partial x$ for the shear d_{xj} in the x-direction can be calculated by processing the phase changes $\Delta\phi_{xj}$ obtained at each camera $j = 1, 2$:

$$\begin{bmatrix}\partial u/\partial x\\ \partial w/\partial x\end{bmatrix} = \frac{\lambda}{2\pi}\begin{bmatrix}k_{x1} & k_{z1}\\ k_{x2} & k_{z2}\end{bmatrix}^{-1}\begin{bmatrix}\Delta\phi_{x1}/d_{x1}\\ \Delta\phi_{x2}/d_{x2}\end{bmatrix} \overset{\substack{\text{if symmetric}\\ \text{setup in } xz-\text{plane}}}{\approx} \frac{\lambda}{4\pi}\begin{bmatrix}1/\sin(\Theta) & 1/\sin(-\Theta)\\ 1/(\cos(\Theta)+1) & 1/(\cos(\Theta)+1)\end{bmatrix}\begin{bmatrix}\Delta\phi_{x1}/d_{x1}\\ \Delta\phi_{x2}/d_{x2}\end{bmatrix}. \quad (2)$$

Eqs(1) and (2) are valid as long as the illumination and the symmetric viewing directions lay in xz-plane. In case of angular misalignment between the viewing directions and the illumination of fewer than 5 degrees (rotation over the x axis), the shear strain $\partial v/\partial x$ is mixed up with the out-of-plane component $\partial w/\partial x$ up to 5% (assuming the magnitude of these components is comparable).

2.1. High-speed shearography

Given the fact that the pulsed illumination at μs time scale is possible with modern lasers that can deliver two or several sub-pulses [50], the main choice is of the camera architecture. A comparison of the different approaches for high-speed shearography is done in Table 1.

In this project, the third architecture with the double frame cameras was chosen due to the ability to achieve high number of pixels and small pixel size as they define the highest spatial frequency and the frequency range, respectively. These are the main limitations of the high-speed cameras in options 1 and 2. The limitation of two frames per camera can be overcome by increasing the number of cameras [56] or by repeating the experiments with controlled delays.

3. Instrument design and development

3.1. Spatial phase-shift shearography

Fig. 2 shows the shearography configuration for one of the cameras with spatial phase-shifting using the Michelson [27] or the double imaging Mach-Zehnder [25] interferometers. Both configurations implement the shearing principle by one of the mirrors which is tilted with respect to the reference one. The spatial phase-shift is realised by slits in both interferometers (Fig. 2 (b,c)) which limit the frequency bandwidth of the recorded interferogram with a cut-off frequency $f_{cut} = D/2\lambda f$ [24], where D is the slit width projected to the focal plane and f is the focal length of the imaging lens. In the case of Michelson interferometer, the filtering is done in the front focal plane of the first lens of the 4f system, in the Mach-Zehnder scheme – this is done directly in the front focal plane of each imaging lens. The offset (carrier) frequency f_o is set by the angular offset β as $f_o = \sin\beta/\lambda$. For the Michelson interferometer

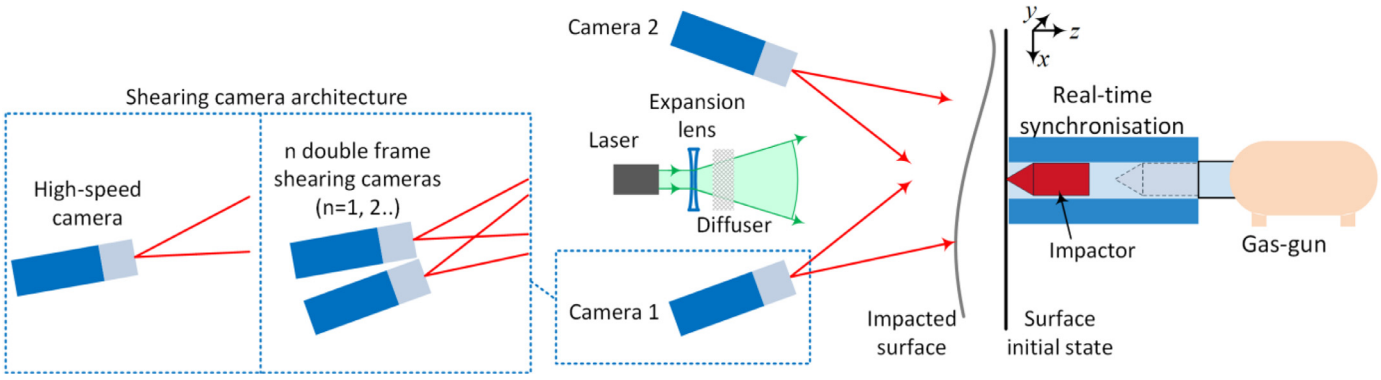

Fig. 1. The EXTREME shearography instrument for in- and out-of-plane measurements.

Table 1
Comparison of the shearing cameras architectures. Parameters may depend on specific camera models.

Camera architecture	Main advantages	Main limitations
1. One or more high-speed cameras with a trade-off between the spatial resolution and the frame rate [51–53]	• Flexibility in various frame rates with a trade-off for the resolution • Ability to capture a sequence of interferograms to record the whole impact event	• Frame rates around 10^6 fps result in low spatial resolution (order of 128×48 pixels), which is not enough for digital speckle interferometry
2. One or more high-speed cameras with a fixed resolution at extremely high frame rates (buffer on the sensor) [55]	• Moderate spatial resolution (close to 1 Mpixel) at extremely high frame rates (higher than $5{\cdot}10^6$ fps) • Ability to capture a sequence of interferograms (up to 100-200 frames)	• [Valid for architectures 1-2] Large pixel size (order of 20×20 μm) and low fill factor limit the maximum spatial • frequencies for the spatial phase-shift • High price, especially if 2 or 3 cameras are needed for the 3D shearography [5,6,54]
3. One or several double frame CCD cameras with an interline frame transfer [18–22,34–40]	• High spatial resolution (several Mpixel) • Small pixel size (up to 3×3 μm) • Affordable price	• The number of frames is limited to 2 per camera • Long exposure time for the second frame if no extra shutter is used (exposure equal to a readout time of the first frame, reaches 100-200 ms)

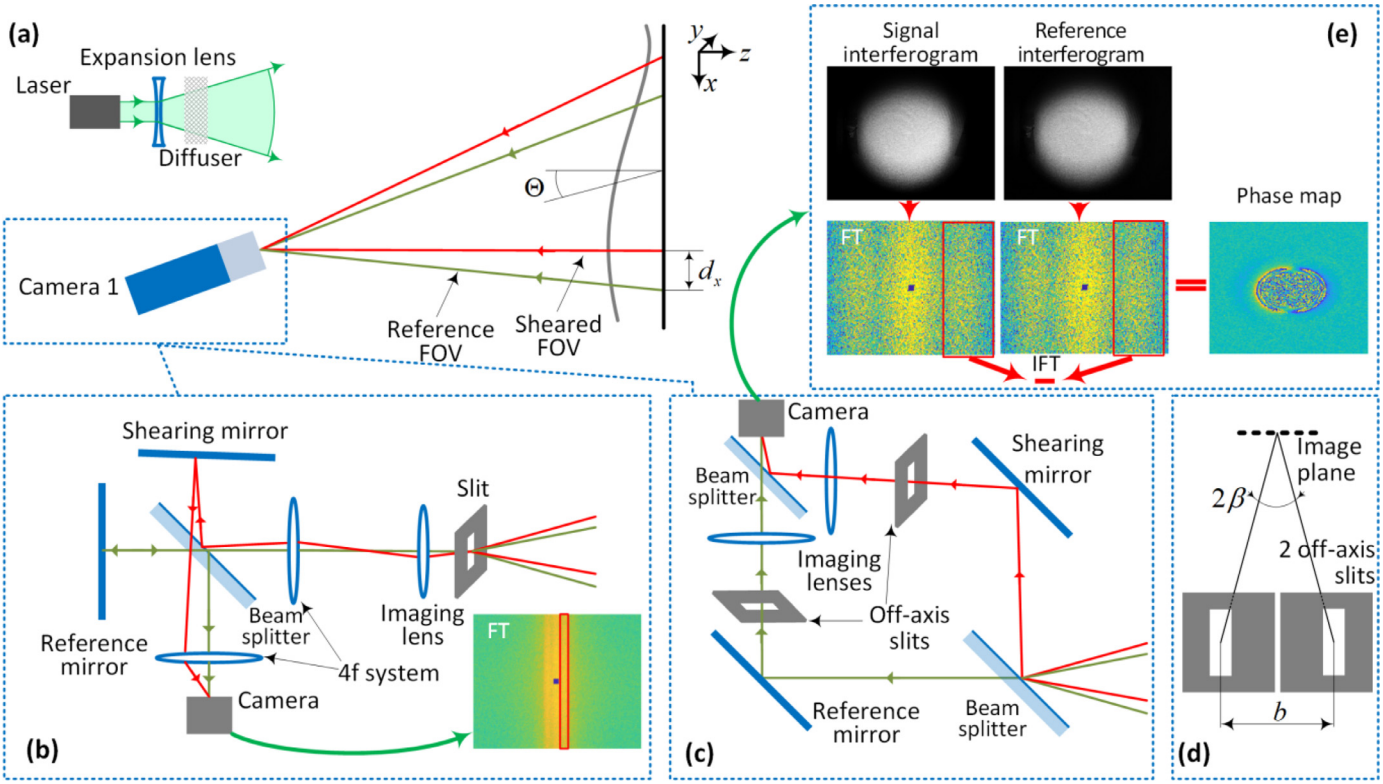

Fig. 2. Shearography configuration (a) for one of the cameras with spatial phase-shifting with modified (b) Michelson or (c) double imaging Mach-Zehnder interferometers: schematic representation of the optical paths in both configurations, (d) relative off-axis offset of the slits in Mach-Zehnder scheme and (e) data processing flow in the Fourier domain (FOV – field of view, FT – Fourier transform, IFT – inverse Fourier transform).

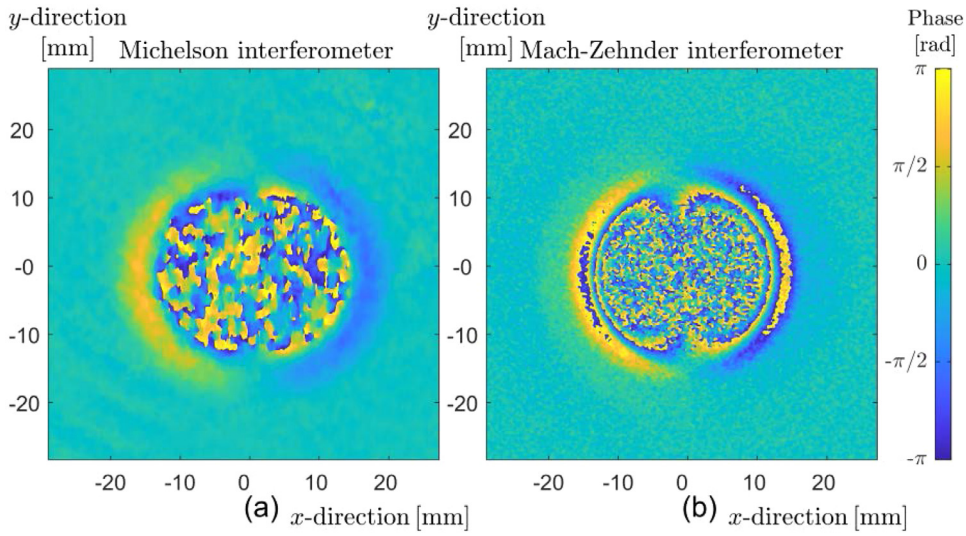

Fig. 3. Comparison of the phase maps captured with (a) the Michelson and (b) Mach-Zehnder interferometers (Fig. 2(b,c), respectively) corresponding to the out-of-plane deformation during impacts on aluminium plates with the shear in the x-direction.

(Fig. 2 (b)), f_o depends on the actual shear amount β expressed in an angular form. For the Mach-Zehnder interferometer, f_o is independently set by the angular offset of the slits β (Fig. 2 (c,d)) [25]. Both interferometers were modified by using a slit instead of circular apertures to improve the energy efficiency and quality of the revealed phase maps by increasing the area and frequency range of the side maximums in the Fourier spectrum (red rectangles in Fig. 2(b,e)) [57].

After the inverse Fourier transformation, the side maximums yield a complex function that contains the phase information ϕ_x^{ref} and ϕ_x' for the interferograms captured before and after the deformation, respectively. To isolate these maximums with a windowed transform, the offset frequency f_o has to be at least twice higher than f_c, i.e. $2f_{cut} \leq f_o \Rightarrow D \leq f \sin\beta$ [24].

The dynamic range of the measured strain during an impact event has to be maximized. For that, the shear distance typically has to be decreased. For the Michelson interferometer this is up to a reliable spectra separation (as in Fig. 2(b)), for the Mach-Zehnder interferometer this is up to the experimentally found limit of not less than 2 speckle sizes. When the slit is used, the speckle size is defined as the longest size of the speckle (here horizontal). To minimize the subjective speckle size $\Delta s = \lambda f / D$, the slit width D has to be maximized. However, the minimum speckle size Δs for shearography has to be more than 6 pixels [24]. This makes the trade-off for the slit width D:

$$\lambda f / 6p_x \leq D \leq f \sin\beta, \tag{3}$$

where p_x is the pixel size in the x-direction. Therefore, for reliable spectral separation, it is preferable to use cameras with a minimal pixel size and a high number of pixels (see option 3 in Table 1).

3.2. Experimental comparison of the interferometers

One Michelson and one Mach-Zehnder interferometers were similarly assembled to experimentally compare their performance. To simplify the preliminary tests, the interferometers were oriented perpendicularly to the object, so the phase maps (Fig. 3) recorded during impact events correspond to the out-of-plane deformation. Each interferometer was tested individually in the same test conditions and impact energy with new aluminium specimens, which is a simple material case. The mean shear distance over the field of view for the Michelson interferometer was decreased to 2.7 mm from the previously reported results [45] up to the limit of the spectra separation (Fig. 2(b)). The Mach-Zehnder interferometer had a shear with the mean value of 1.4 mm.

The phase maps (Fig. 3) reveal the propagation of a symmetric circular flexural wave during the time interval around 3 to 4 μs after the moment of the impact. Fig. 3(b) was captured with the Mach-Zehnder interferometer and reveals the increased dynamic range of the resolved phase fringes in comparison with the Michelson interferometer. According to the comparison of the shear distances, the Michelson interferometer is expected to have a higher phase value (more fringes, Eq. (1)), however, these fringes are not resolved in the phase map.

For accurate strain estimation over the field of view (Eq. (2)) two corrections have to be implemented. First, the sensitivity vector has to be corrected due to the varying viewing angle Θ for different points of the specimen [5,6]. Second, the non-uniformity of the shear distance has to be calibrated, e.g. by capturing an object with a known 2D pattern via reference and sheared field of views. Fig. 4 shows the shear distance variation for both interferometers when checkerboard images were captured independently through the reference and the sheared field of view and the relative shifts of all corners were identified and interpolated [54].

Fig. 4 shows that both interferometers have non-uniform shear distances which is a cumulative result of the misalignments and imperfections of the specific optical parts (e.g. mirrors non-flatness). According to Fig. 4, the distributed optical scheme in a Mach-Zehnder interferometer may result in a 15% difference over the field of view in comparison with 1% with the Michelson one. In case of the impact-monitoring when the optical setup is located close to the impact event, a final alignment of the setup after each impact is challenging, therefore according to our practice, the post-calibration of the actual shear amount is preferable and easier implemented than the optics realignment.

3.3. EXTREME shearography instrument design

Based on the performance comparison of the two interferometers (Figures 3 and 4), the architecture with the Mach-Zehnder interferometer was used further for the instrument development. This is mainly due to the ability to adjust the shear distance independently from the offset frequency which is critical for the high strain scenario as an impact event. To maximise the coupling of the experimental data with the numerical models, the developed configuration of the shearography instrument (Fig. 5) realises measurements of the in- and out-of-plane surface strain components ($\partial u/\partial x$ and $\partial w/\partial x$ or $\partial v/\partial y$ and $\partial w/\partial y$ depending on the shear direction during the impact, Eq. (2)). Therefore two shearing interferometers were placed symmetrically in a horizontal plane. The instrument was built together with a gas-gun as an impact chamber with three zones driven by the safety measures:

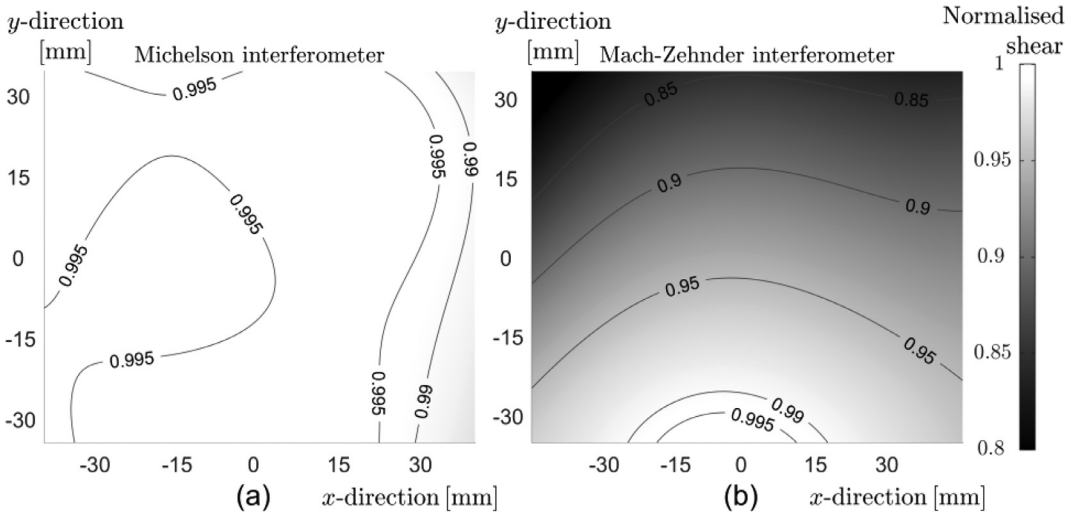

Fig. 4. Variation of the shear distance in the x-direction for (a) the Michelson and (b) Mach-Zehnder interferometers (Fig. 2(b, c)). The shear values were normalized for a direct comparison.

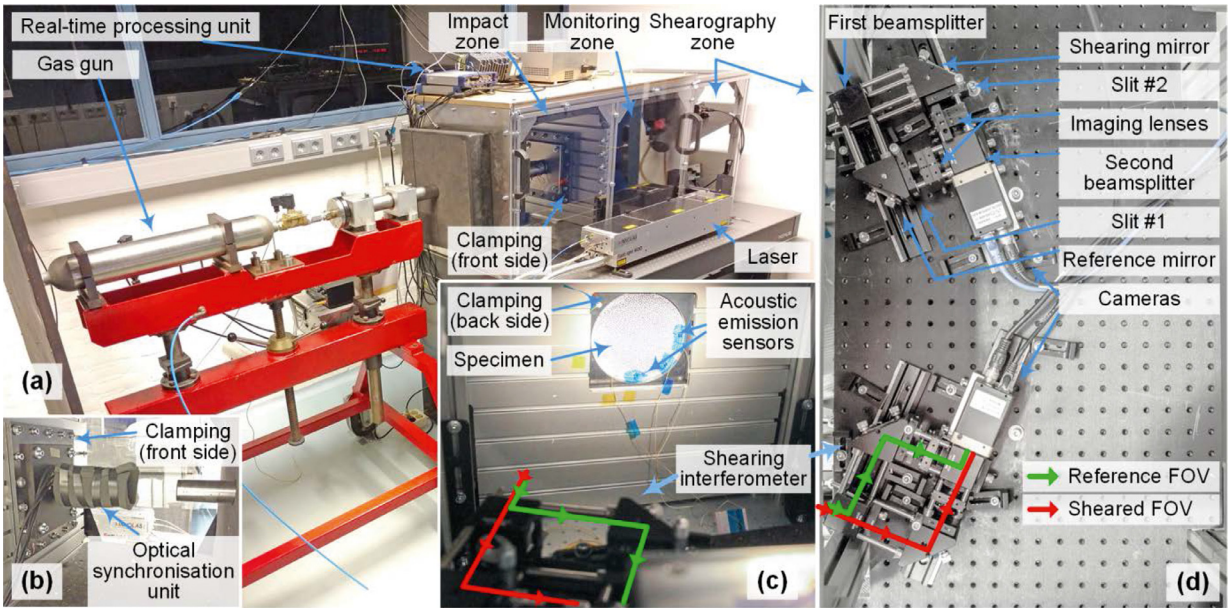

Fig. 5. EXTREME shearography instrument for in- and out-of-plane surface strain measurements:
(a) overview of the instrument, the gas-gun and the impact chamber,
(b) the impact zone with the specimen clamping and the optical synchronisation unit,
(c) the monitoring zone as seen from one of the shearing interferometers,
(d) two symmetric shearing interferometers implementing the double-imaging scheme.

a) an impact zone with the optical synchronisation unit providing real-time information about the approaching impactor (Fig. 5(b));
b) a monitoring zone where the back surface of the specimen is observed during the impact (Fig. 5(c));
c) a shearography zone where the shearing cameras and the laser beam path are placed (Fig. 5(d)).

The gas-gun is adapted for impact speeds up to 200 m/s and operates under pressurised air or nitrogen, impact release is controlled by an electromagnetic valve. The impactor design with a hemisphere tip with a radius of curvature of 5 mm was used following standard practice in the aerospace industry.

Each double-imaging Mach-Zehnder interferometer [25] consists of a double-frame camera BOBCAT B3420 by Imperx. This camera has an interline frame transfer with a resolution of 3388×2712 pixels, a pixel size of 3.69×3.69 μm and an interframing time of 200 ns. The speckle pattern is produced by illuminating the specimen with an expanded beam from a pulsed laser in a double pulse regime (customised SpitLight 600 Nd:YAG-Lasersystem by InnoLas Laser GmbH, wavelength 532 nm). An additional ground glass diffuser (Fig. 1(a)) is used to normalise the energy distribution over the illuminated area to overcome the initial circular fringes in the beam due to complex modes combination. Two portions of the single pulse with the initial energy from 100 up to 500 mJ sequentially illuminate the specimen under the control of a Pockels cell with the minimum separation time of 1 μs. In each interferometer, two slits were placed at the front focal planes of the imaging lenses to achieve a better quality of the phase maps in comparison with a circular aperture [57]. The trade-off between the interferometer parameters (Eq. (3)) was made as follows:

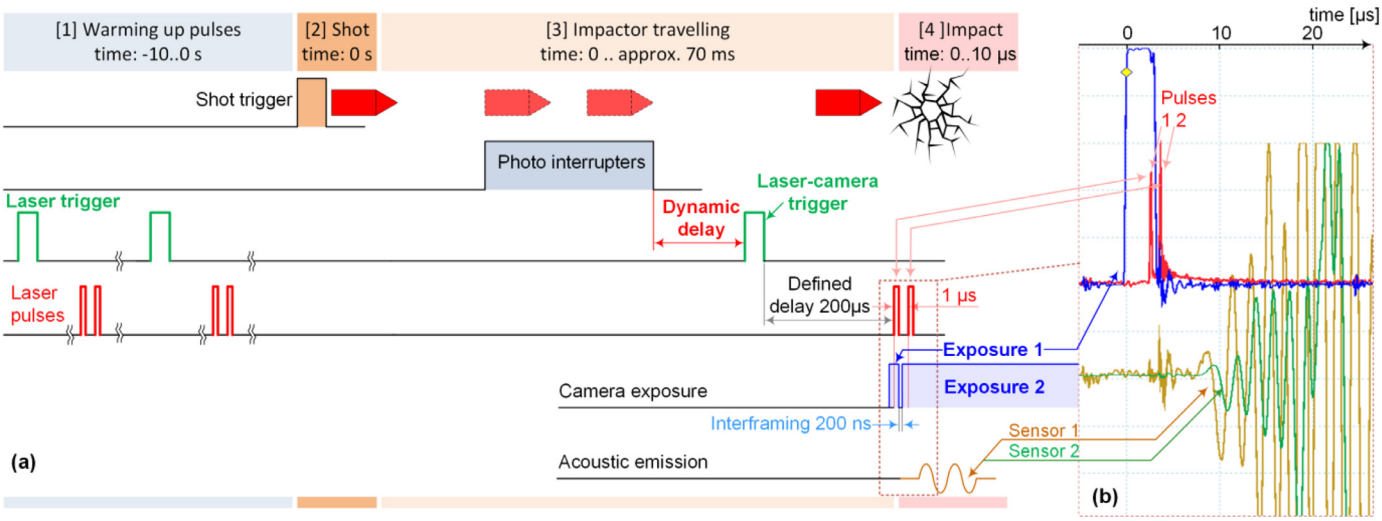

Fig. 6. Timing of the shooting routine: (a) diagram with the main triggers and signals (time scale is not linear), (b) electrical signals captured during an impact: camera exposure (blue line), laser pulses (red) and AE signals (brown and green; time axis is to scale).

a) the minimum distance between the camera and the object of 500-600 mm was based on safety measures;
b) the focal length was maximised up to 50 mm (Xenoplan 2.8/50 by Schneider) and defined by the visible area of Ø150 mm;
c) each slit was shifted from the joint axis by 1.9 mm (β=2.3°) resulting in the offset frequency close to a half of the maximum one, see Fig. 2 (c-e);
d) the 1.8 mm slit was chosen as a rational compromise resulting in the absence of the overlap of the central and side maximums of the Fourier spectra and the average subjective speckle size of 7 pixels (corresponding to 0.35 mm; along with the x-axis).
e) the shear distance d_x was decreased in comparison with the preliminary tests (section 3.2) to 17 to 21 pixels (0.9..1.1 mm) and calibrated over the field of view for both cameras as in Fig. 4(b).

During the tests, square specimens of 200×200 mm are tightly clamped between two square clamps with circular windows on both impact and observing sides (Fig. 5(b, c)). The clamping itself is fixed to the wall which divides the impact and monitoring zones. To improve the laser light scattering, the specimens are painted with matte white paint.

3.4. *"On-the-fly" synchronisation based on the approaching impactor*

Missing the impact means loss of the specimen, therefore all parts of the instrument require reliable real-time synchronisation with an accuracy up to 1 μs to capture the initial moment of impact. The overall shooting procedure takes more than 10 seconds (Fig. 6(a)) and includes: phase 1. Warming: 10 s of pre-heat of the laser for thermal stabilisation by triggering the laser (green signal in Fig. 6(a)) resulting in 100 double pulses (red signal) at 10 Hz; phase 2. Shot: opening of the gas-gun valve, the impactor starts travelling; phase 3. Travelling: the impactor travels towards the specimen being continuously monitored by the optical interrupters to calculate the expected impact time and the needed "dynamic delay" before the final "laser-camera" trigger; phase 4. Impact: capturing of two frames synchronously with two laser sub-pulses and acoustic emission (AE) signals from two sensors (Fig. 5(c)).

"On-the-fly" synchronisation is done by processing signals from 20 optical interrupters (pairs of LED and fast phototransistors) which cross the path of the impactor (Fig. 5(b)) using a real-time processing unit with an FPGA architecture [45,46]. The actual speed of the impactor is calculated based on the relative delays between these 20 signals, then the appropriate delays to trigger the laser and the camera are calculated in a real-time right before the impact. After the impact, the actual moment of impact is estimated by processing signals (brown and green in Fig. 6(b)) from two miniature acoustic emission sensors PICO HF-1.2 by Physical Acoustics operating in the range of 500-1850 kHz which are taped directly to the specimen symmetrically from the specimen center (Fig. 5(c)).

4. Experimental results

The experimental results presented here are to investigate the instrument performance. For that two aerospace grade materials were selected with isotropic and anisotropic properties. A separate study will cover the modelling aspect of the material behaviour.

The developed instrument with the Mach-Zehnder architecture was used for the main tests. The in- and out-of-plane surface strain components were measured during impact tests on 4 mm thick 6082-T6 aluminium specimens (Fig. 7) and 3 mm thick carbon fibre reinforced composite (CFRP) specimens with 0/90/0/90/0 layup of unidirectional plies (Fig. 8). The strain maps reveal the evolution of $\partial u/\partial x$ and $\partial w/\partial x$ in between the laser pulses (1 μs, Pockels cell separation time) with varying delay starting from the moment of the impact and not the total strain which was built up during the impact. Each impact experiment with a new specimen resulted in a pair of maps ($\partial u/\partial x$ and $\partial w/\partial x$) presented in sub-columns in Figures 7 (e.g. a and e in the red rectangle, b and f, etc.) and 8. Strain components $\partial v/\partial y$ and $\partial w/\partial y$ in Fig. 8 were measured by rotating the specimens by 90 degrees and maintaining the same calibrated shear distance d_x. Note the phase unwrapping algorithm has not been able to resolve all fringes and fully identify all the phase steps, which resulted in the partially lost data.

The impactor and the damage in the CFRP specimen are shown in Fig. 9. No penetration of the impactor was observed in the CFRP and aluminium specimens. During the tests, the impactor speed was in the range of 58.5±0.5 m/s corresponding to a 53.8..55.7 J impact energy range with an impactor of 32 g.

The strain maps in Figures 7 and 8 reflect both spatial and temporal information on the flexural waves. To assess the temporal aspect, the wave speeds for the aluminium specimens (Fig. 7) were estimated, first, based on the AE signals recorded by the piezo-electric sensors and then compared with the one derived from the graphically captured strain maps (Fig. 7). For both cases, the cross-sections of the strain maps were plotted together in Fig. 10 and matched with the AE signals from the same tests (shown on the left and right sides). First, the speed of 5490 m/s was calculated by averaging the time of arrival of the wave to

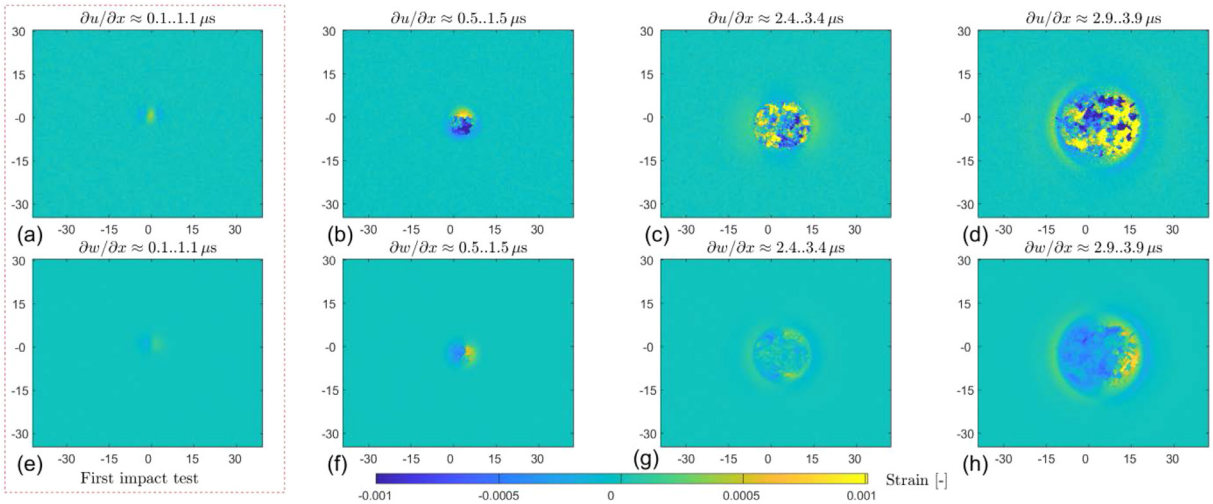

Fig. 7. In- and out-of-plane surface strain maps ($\partial u/\partial x$ and $\partial w/\partial x$) of 4 mm aluminium plates (6082-T6) at the time from 0 to 2.9..3.9 μs after the impact. Axes units mm.

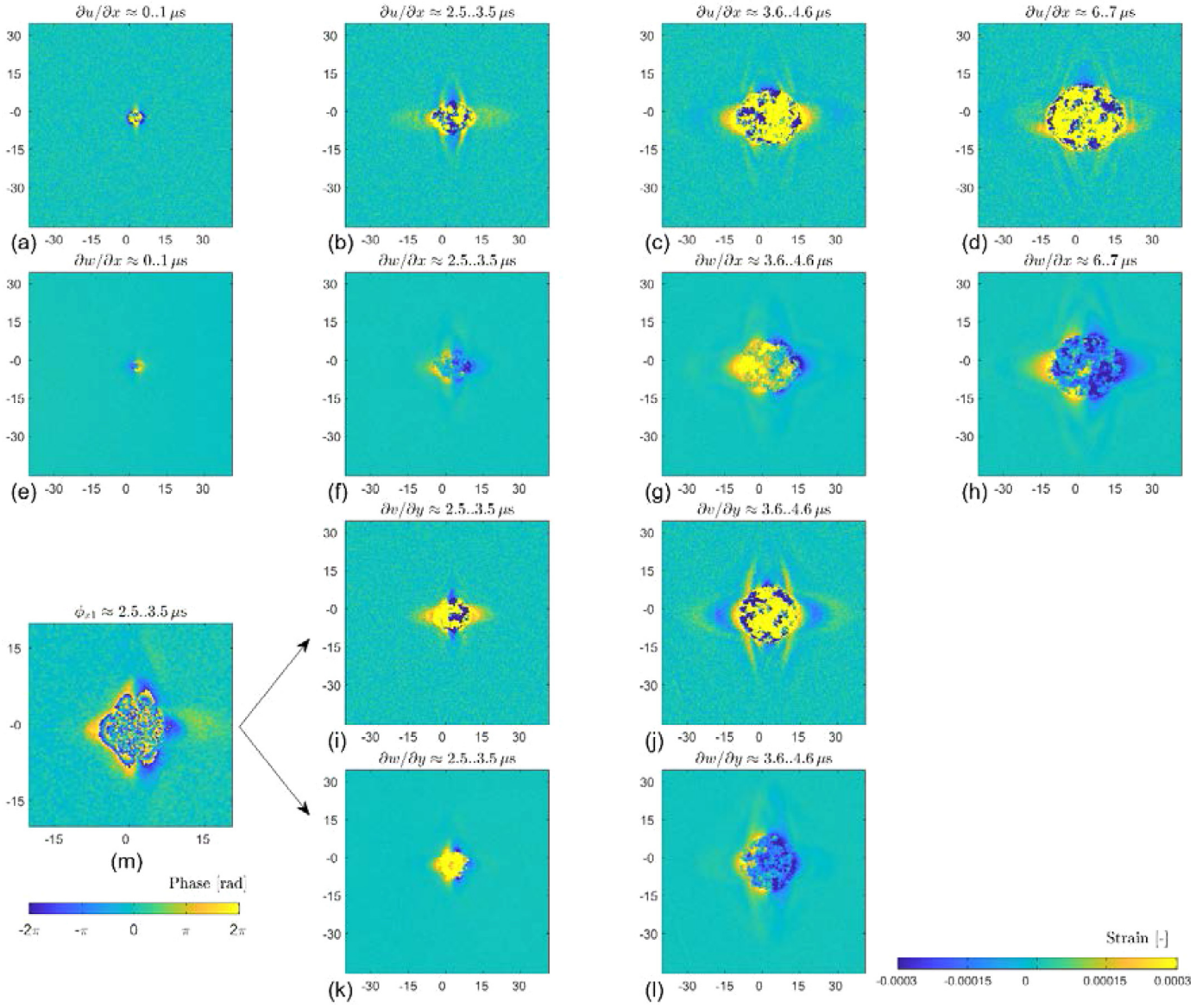

Fig. 8. In- and out-of-plane surface strain maps ($\partial u/\partial x$ and $\partial w/\partial x$, $\partial v/\partial y$ and $\partial w/\partial y$) of 3 mm CFRP specimens at the time from 0 to 6..7 μs after the impact with an additional zoom (m) into the unwrapped phase map. Axes units mm.

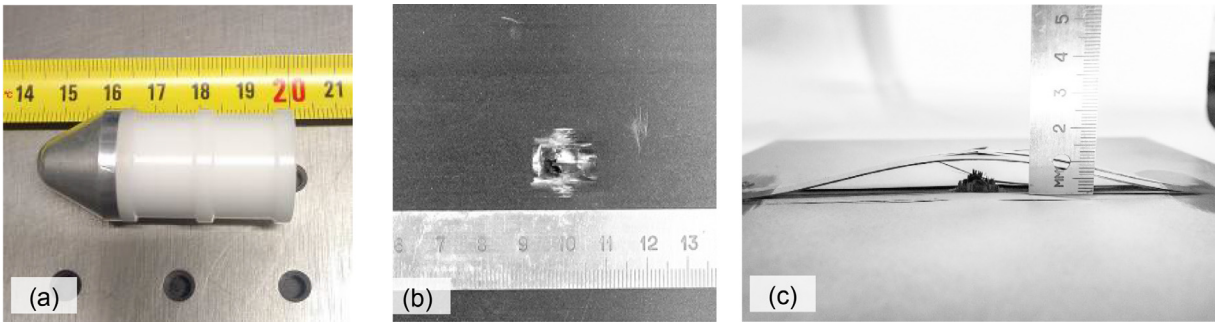

Fig. 9. The impactor (a), (b) the impacted and (c) the monitored side of the 3 mm CFRP specimen revealing the damage after the impact.

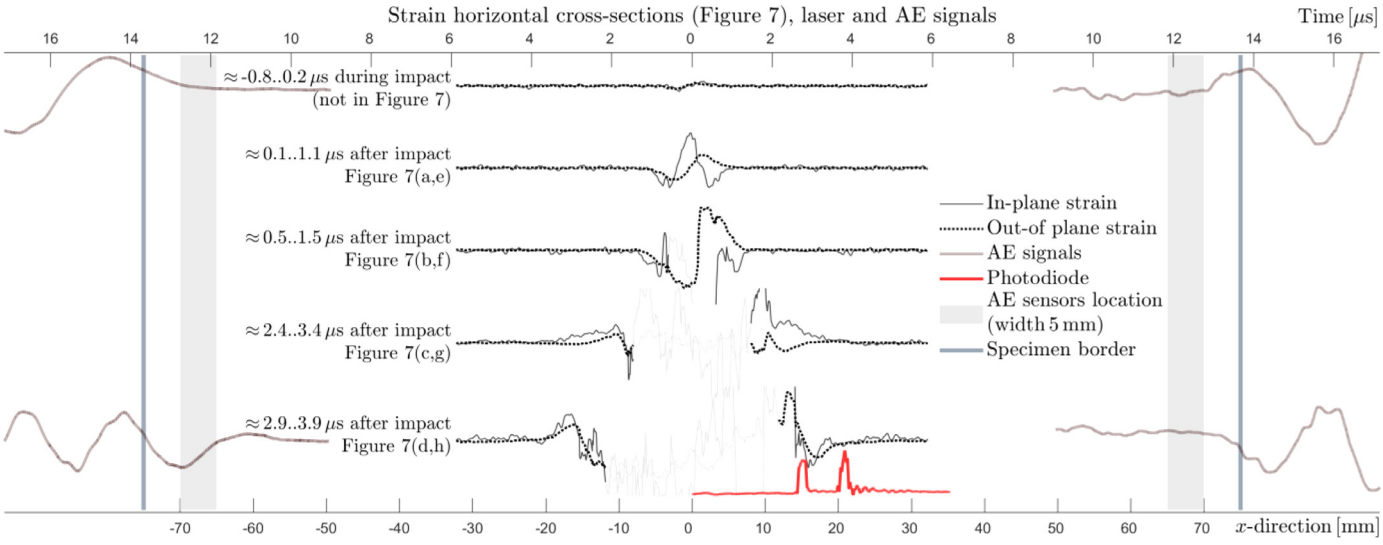

Fig. 10. Matching the geometrical and time data: cross-sections of the strain maps per impact from Figure 7, the signals from a photodiode and the acoustic emission (AE) sensors captured during the impact events. The unresolved strain values are plotted in light grey colour.

the AE sensors placed symmetrically between 65 and 70 mm (grey area) from the specimen center during the first impact test (top line in Fig. 10). This value was used to recalculate the spatial x-axis in mm (bottom) to the time axis (top). The second calculation was done based on the location of the wavefront in the captured strain maps (lines two to five) with an assumption, that the speed of the graphically captured wave may differ from the measured with AE signals. Four cross-sections from 1.1 to 3.9 μs were averaged to give the speed estimation of 5380 m/s, which differs by 2% from the value measured with the AE sensors.

Two photodiode signals (red line in Fig. 10; shown only for one experiment) with 1 μs separation time represent the laser sub-pulses recorded during the impact (also in Fig. 6(b)) together with the AE signals (plotted at the same time scale). Once the cross-sections of strain maps were matched with the corresponding time (top and bottom axes), the rising edge of the second photodiode signal (second sub-pulse) corresponds to the location of the wavefront in the spatial domain.

5. Discussion

The first strain maps in Figures 7 and 8 (a,e; b,f) and 5 (a,e) reveal the elastic response of the material during the initiation of the impact event during the first 0..2 μs after the impact. Further in time, the propagation of the flexural wave is observed at varying delays after the impact. For the aluminium specimens (Fig. 7), the expected axial symmetric waves were observed. The wavefront for the composite specimens (Fig. 8) reveals the anisotropy of the material properties resulting in different wave velocities in different directions. The waves travel faster along the reinforcement fibre directions (vertical and horizontal) and slower in the diagonal directions [58,59]. The measured strain maps will be used as one of several validation techniques for the new numerical and analytical models being developed within the EXTREME project [2,3,47]. For composites, this information about the early response may supplement the failure modes analysis (fibre or matrix fracture, delamination, plasticity).

The estimated speed of the captured waves of 5380-5490 m/s (Fig. 10) is smaller than the expected 6240 m/s (speed of the longitudinal ultrasonic wave for 6082-T6 aluminium calculated with Young's modulus 71 GPa, Poisson's ratio 0.33, density 2700 kg/m^3). The difference can be explained by the uncertainties in the estimation of the time of arrival (about ±0.5 μs), the moment of the actual impact, sensor positioning error (±1 mm), repeatability of the impact location (±2-3 mm) and the repeatability of the tests in general. Further investigation is needed to identify the modal composition of the emerging acoustic waves.

The aforementioned repeatability of the tests is a crucial issue. The comparison of the strain maps in Figures 7,8, and 10 is based on the condition that was made, that the tests are repeatable and reproducible. In a general case, they are not due to varying impactor speed of 58.5±0.5 m/s and corresponding impact energy of 53.8..55.7 J (due to varying pressure in the gas gun vessel), variation of the material properties, specimen geometries and other experimental conditions. However, the instrument and the experimental procedure were designed and developed in a way to minimize these deviations. In our experiments, the desired delay between the impact and the laser sub-pulses could differ from the actual one by up to several microseconds. However, the recorded time data of the travelling impactor, triggers, laser sub-pulses

and AE signals allowed us to post-calculate and reconstruct the actual timing with the uncertainty of around ±0.5 μs.

The main problem of the captured phase maps and further calculated strain maps is the loss of the measurement results in the center after 2-3 μs (depending on the material properties). This happens because of a high number of fringes at the impact location in a butterfly pattern, which is characteristic for shearography. Fig. 8(m) shows a filtered wrapped phase map from one of the cameras where the symmetric butterfly pattern can be identified. Later the unresolved fringes at the center are clustered during the unwrapping procedure which results in the lost data. Based on our experience [45,46] the overall dynamic range of the presented Mach-Zehnder scheme is improved in comparison with the Michelson configuration. Further improvements could be:

a) increasing the laser wavelength from 532 nm to 1064 to double the dynamic range of the recording surface strain, however, attention has to be paid to the decreased by a half speckle size;
b) increasing the focal length of the imaging lenses to increase the spatial resolution (Eq. (3)), but limiting the field of view.

An alternative approach is to investigate the capabilities of ESPI to monitor the presented impact scenario. According to the experimental results [18–22], the phase maps obtained with ESPI often have more resolved fringes than with shearography. However, according to our experience, the required alignment of the optical setup after each impact test may be challenging.

An additional technical comment has to be made about the double imaging Mach-Zehnder interferometer [25] in comparison with the Michelson scheme. The beam splitter that has to be placed behind the imaging lenses (Fig. 2(c)) causes practical difficulties in the use of standard C/CS mount objective lenses and single lenses with short focal lengths (less than 30 mm) in combination with standard C/CS mount cameras. This is because of the gap between the last mechanical part of the objective lens and the image plane of the camera sensor has to be at least 16.7 mm which corresponds to the reduced thickness of a 1-inch prism in air. When additional margins for the mechanical assembly, in practice 10-20 mm are taken into account, the required gap is more than 30 mm. This makes most of the standard C-mount objective lenses not applicable for this task (as the back focal distance is 16 mm). As a solution, single lenses with the focal length of more than 25-30 mm can be used with the expected poor image quality. The objective lens used in this project (Xenoplan 2.8/50 by Schneider) together with the camera (BOBCAT B3420 by Imperx) have high integration capability by partial disassembly of the parts which retains the appropriate image quality.

6. Conclusions

In this paper, the design, development and experimental results of a new shearography instrument for high-speed impact monitoring are presented. The new instrument is capable of capturing the impact response of materials using two recently reported configurations of shearing interferometers which were adapted and experimentally compared. The double imaging Mach-Zehnder configuration was used for the final design due to the independent adjustment of the shear amount, which is the key parameter to be minimized when high strain values are expected.

The main value of the presented experimental results is in the μs mapping of the flexural waves during the first moment after the impact. As expected, waves with the axial symmetry were captured for aluminium specimens, and axially asymmetric for the composites. Further analysis of the wavefronts will be used as input and validation data for new numerical and analytical models of the impact response of composites and for validation of other experimental techniques as acoustic emission and embedded piezo sensors [49]. Currently, the EXTREME shearography instrument realises measurements of the in- and out-of-plane surface strain components during the impact using the double frame approach. The overall set of technical parameters of the developed shearography instrument makes it one of the most extreme applications of shearography for material characterisation.

Future steps of the instrument development include optimisation of the interferometer to increase its dynamic range, exploring simultaneous measurements in multiple sharing directions [60] and recording of a sequence of interferograms (more than 2) in a “pulse train” regime. The material behaviour during the impact will be numerically modelled and compared with the experimental results.

Funding statement

The project “EXTEME” leading to this paper has received funding from the European Union’s Horizon 2020 research and innovation program under agreement No. 636549.

Declaration of Competing Interest

The authors declare that they have no known competing financial interests or personal relationships that could have appeared to influence the work reported in this paper.

Supplementary materials

Supplementary material associated with this article can be found, in the online version, at doi:10.1016/j.optlaseng.2020.106502.

CRediT authorship contribution statement

Andrei G. Anisimov: Methodology, Software, Investigation, Validation, Writing - original draft. **Roger M. Groves:** Conceptualization, Validation, Supervision, Funding acquisition, Writing - review & editing.

References

[1] Robin O. Mass criterion for wave controlled impact response of composite plates. Compos Part A Appl Sci Manuf 2000;31(8):879–87.
[2] Vignjevic R, Djordjevic N, De Vuyst T, Gemkow S. Modelling of strain softening materials based on equivalent damage force. Comput Methods Appl Mech Eng 2018;335:52–68.
[3] Giannaros E, Kotzakolios A, Sotiriadis G, Tsantzalis S, Kostopoulos V. “On fabric materials response subjected to ballistic impact using meso-scale modeling. Numerical simulation and experimental validation,”. Compos Struct 2018;204:745–54.
[4] Hung YY. Shearography: a new optical method for strain measurement and non-destructive testing. Opt Eng 1982;21:213391.
[5] Steinchen W, Yang L. [Digital shearography]. Bellingham, Washington: SPIE Press; 2003.
[6] Francis D, Tatam RP, Groves RM. Shearography technology and applications: a review. Meas Sci Technol 2010:29 21, 102001.
[7] Hung YY. Shearography for non-destructive evaluation of composite structures. Opt Lasers Eng 1996;24(2-3):161–82.
[8] Hung YY. Applications of digital shearography for testing of composite structures. Compos B Eng 1999;30(7):765–73.
[9] Kim G, Hong S, Jhang KY, Kim GH. NDE of low-velocity impact damages in composite laminates using ESPI, digital shearography and ultrasound C-scan techniques. Int J Precis Eng Manuf 2012;13(6):869–76.
[10] Ochôa P, Infante V, Silva JM, Groves RM. Detection of multiple low-energy impact damage in composite plates using Lamb wave techniques. Compos B Eng 2015;80:291–8.
[11] Goto DT, Faraz MI, Rans CD, Groves RM. Low energy impact damage detection using shearography. Proc Photomech 2011.
[12] Okafor AC, Otieno AW, Dutta A, Rao VS. Detection and characterization of high-velocity impact damage in advanced composite plates using multi-sensing techniques. Compos Struct 2001;54(2-3):289–97.
[13] Lee JR, Molimard J, Vautrin A, Surrel Y. Application of grating shearography and speckle shearography to mechanical analysis of composite material. Compos Part A Appl Sci Manuf 2004;35(7-8):965–76.
[14] Lomov SV, Ivanov DS, Verpoest I, Zako M, Kurashiki T, Nakai H, Molimard J, Vautrin A. Full-field strain measurements for validation of meso-FE analysis of textile composites. Compos Part A Appl Sci Manuf 2008;39(8):1218–31.
[15] Anisimov AG, Müller B, Sinke J, Groves RM. Analysis of thermal strains and stresses in heated fibre metal laminates. Strain 2017;54:1–16.
[16] Fällström K-E, Gustavsson H, Molin N-E, Wåhlin A. Transient bending waves in plates studied by hologram interferometry. Exp Mech 1989;29(4):378–87.
[17] Fällström K-E, Lindgren L-E, Molin N-E. Transient bending waves in anisotropic plates studied by hologram interferometry. Exp Mech 1989;29(4):409–13.
[18] Schedin S, Gren P. Phase evaluation and speckle averaging in pulsed television holography. Appl Opt 1997;36(17):3941–7.

[19] Field JE, Walley SM, Proud WG, Goldrein HT, Siviour CR. Review of experimental techniques for high rate deformation and shock studies. Int. J Impact Eng 2004;30(7):725–75.
[20] Schmidt A. “Experimental investigations on nondestructive testing methods for defect detection with double-pulse electronic speckle pattern interferometry,”, Hamburg, Germany: Helmut-Schmidt-University / University of the Federal Armed Forces; 2009. PhD Thesis.
[21] Diaz FV, Kaufmann GH. Impact-induced transient deformation analysis by means of digital speckle pattern interferometry. Exp Mech 1999;39(4):311–16.
[22] Lopes H, Guedes RM, Vaz MAP, Rodrigues JD. Study of transient wave propagation in plates using double pulse TV holography. In: Proc. international conference on advances in computational and experimental engineering and sciences; 2004. p. 2216–21.
[23] Yang L, Xie X. [Digital shearography: new developments and applications]. Bellingham, Washington: SPIE Press; 2016.
[24] Pedrini G, Zou YL, Tiziani HJ. Quantitative evaluation of digital shearing interferogram using the spatial carrier method. Pure Appl Opt A 1996;5(3):313.
[25] Gao X, Yang L, Wang Y, Zhang B, Dan X, Li J, Wu S. Spatial phase-shift dual-beam speckle interferometry. Appl Opt 2018;57(3):414–19.
[26] Gao X, Wang Y, Dan X, Sia B, Yang L. Double imaging Mach-Zehnder spatial carrier digital shearography. J Mod Opt J Mod Opt 2019;66(2):153–60.
[27] Xie X, Yang L, Xu N, Chen X. Michelson interferometer based spatial phase shift shearography. Appl Opt. 2013;52(17):4063–71.
[28] Xie X, Li J, Zhang B, Yan L, Yang L. Improvement of phase map quality for Michelson interferometer based spatial phase-shift digital shearography. Asian J Phys 2015;24(10):1391–400.
[29] Aranchuk V, Lal AK, Hess CF, Trolinger JD, Scott E. Pulsed spatial phase-shifting digital shearography based on a micropolarizer camera. Opt Eng 2018;57(2):024109.
[30] Fu Y, Pedrini G, Hennelly BM, Groves RM, Osten W. Dual-wavelength image-plane digital holography for dynamic measurement. Opt. Lasers Eng 2009;47(5):552–7.
[31] García BB, Moore AJ, Pérez-López C, Wang L, Tschudi T. Spatial phase-stepped interferometry using a holographic optical element. Opt Eng 1999;38(12):2069–74.
[32] Moore AJ, Hand DP, Barton JS, Jones JDC. Transient deformation measurement with electronic speckle pattern interferometry and a high-speed camera. Appl Opt 1999;38:1159–62.
[33] Steinchen W, Yang LX, Kupfer G, Maeckel P, Voessing F. Toward double-pulse digital shearography. In: Advances in optical beam characterization and measurements 3418; 1998. p. 19–27.
[34] Spooren R, Dyrseth AA, Vaz M. Electronic shear interferometry: application of a (double-) pulsed laser. Appl Opt 1993;32(25):4719–27.
[35] Chen F, Luo WD, Dale M, Petniunas A, Harwood P, Brown GM. High-speed ESPI and related techniques: overview and its application in the automotive industry. Opt Lasers Eng 2003;40(5-6):459–85.
[36] Francis D. Surface strain measurement using pulsed laser shearography with fiber-optic imaging bundles, Cranfield, UK: Cranfield University; 2008. PhD Thesis.
[37] Pedrini G, Pfister B, Tiziani H. Double pulse-electronic speckle interferometry. J Mod Opt 1993;40(1):89–96.
[38] Pedrini G, Tiziani HJ. Double-pulse electronic speckle interferometry for vibration analysis. Appl Opt 1994;33(34):7857–63.
[39] Santos F, Vaz M, Monteiro J. A new set-up for pulsed digital shearography applied to defect detection in composite structures. Opt Lasers Eng. 2004;42(2):131–40.
[40] Shim VPW, Toh SL, Quah SE. Impact-induced flexural waves in a Timoshenko beam – Shearographic detection and analysis. Exp Mech. 1994;34(4):340–8.
[41] Xie X, Lee CP, Li J, Zhang B, Yang L. Polarized digital shearography for simultaneous dual shearing directions measurements. Rev Sci Instrum 2016;87(8):083110.
[42] Zhang B, Xu W, Li J, Siebert T, Yang L. Modified Michelson interferometer based dual shearing single camera digital shearography. Exp Tech 2020;44(2):187–95.
[43] Wang Y, Gao X, Xie X, Wu S, Liu Y, Yang L. Simultaneous dual directional strain measurement using spatial phase-shift digital shearography. Opt Lasers Eng 2016;87:197–203.
[44] Yan P, Sun F, Dan X, Zhao Q, Wang Y, Lu Y. Spatial phase-shift digital shearography for simultaneous measurements in three shearing directions based on adjustable aperture multiplexing. Opt Eng 2019;58(5):054105.
[45] Anisimov AG, Groves RM. EXTREME shearography: development of a high-speed shearography instrument for measurements of the surface strain components during an impact event. Proc SPIE 2018;10834 108340X.
[46] Anisimov AG, Groves RM. EXTREME shearography: high-speed shearography instrument for in-plane surface strain measurements during an impact event. Proc SPIE 2019;11056 110560J.
[47] ”EXTREME dynamic loading – pushing the boundaries of aerospace composite material structures,” www.extreme-h2020.eu (26 June 2020).
[48] Elmahdy A, Verleysen P. Tensile behavior of woven basalt fiber reinforced composites at high strain rates. Polym Test 2019;76:207–21.
[49] De Simone ME, Cuomo S, Ciampa F, Meo M, Nitschke S, Hornig A, Modler N. Acoustic emission localization in composites using the signal power method and embedded transducers. Proc SPIE 2019;10971 109711O.
[50] Nösekabel EH, Honsberg W, Kelnberger R. Development and application of a 10 Hz Nd:YAG double pulse laser for vibration measurements with double pulse ESPI. In: Fringe 2009. Berlin: Springer; 2009. p. 1–6.
[51] Helfrick MN, Niezrecki C, Avitabile P, Schmidt T. 3D digital image correlation methods for full-field vibration measurement. Mech Syst Signal Process 2011;25(3):917–27.
[52] Lagny L, Montresor S, Gautier F, Pezerat C, Picart P. Full field holographic vibrometry at ultimate measurement limits. Digital holography and three-dimensional imaging, M4B-1, optical society of America; 2019.
[53] Picart P, Poittevin J, Gautier F, Pezerat C. Full-field investigation of traveling acoustic waves with digital holography. In: Inter-noise and noise-con congress and conference proceedings, 257; 2018. p. 229–38.
[54] Anisimov AG, Serikova MG, Groves RM. 3D shape shearography technique for surface strain measurement of free-form objects. Appl Opt 2019;58(3):498–508.
[55] Crooks J, Marsh B, Turchetta R, Taylor K, Chan W, Lahav A, Fenigstein A. Kirana: a solid-state megapixel uCMOS image sensor for ultrahigh speed imaging. Proc SPIE 2013;8659:865903.
[56] “pco.dicam C4 4-channel intensified sCMOS camera,” https://www.pco.de/intensified-cameras/pcodicam-c4 (26 June 2020).
[57] Xie X, Li J, Zhang B, Yan L, Yang L. Improvement of phase map quality for Michelson interferometer based spatial phase-shift digital shearography. Asian J Phys 2015;24(10):1391–400.
[58] Fällström K-E, Gustavsson H, Molin N-E, Wåhlin A. Transient bending waves in plates studied by hologram interferometry. Exp Mech 1989;29(4):378–87.
[59] Fällström K-E, Lindgren L-E, Molin N-E. Transient bending waves in anisotropic plates studied by hologram interferometry. Exp Mech 1989;29(4):409–13.
[60] Wang S, Dong J, Pöller F, Dong X, Lu M, Bilgeri LM, Jakobi M, Salazar-Bloise F, Koch AW. Dual-directional shearography based on a modified common-path configuration using spatial phase shift. Appl Opt 2019;58(3):593–603.

Dr Andrei G. Anisimov is a Senior Researcher in Optical Metrology at Delft University of Technology, The Netherlands. He obtained MS and PhD degrees in optical engineering from University ITMO, Russia. In 2014 he joined the Aerospace NDT Laboratory at TU Delft. His research interests include machine vision and laser interferometry techniques for high precision measurement and non-destructive testing of aerospace and civil engineering materials and structures. Current projects include characterization of composite materials, evaluation of damage and structural behaviour.

Dr Roger M. Groves is Associate Professor in Aerospace NDT/SHM and Heritage Diagnostics at Delft University of Technology, The Netherlands. His PhD is in Optical Instrumentation from Cranfield University (2002) and he was a Senior Scientist at Institute for Applied Optics, University of Stuttgart, before joining TU Delft in 2008 as an Assistant Professor. Dr Groves heads a team of approximately 20 researchers in the Aerospace NDT Laboratory at TU Delft. His research interests are Optical Metrology, Fibre Optic Sensing and Ultrasonic Wave Propagation in Composite Materials. He has approximately 200 journal and conference publications in these topics. In 2020 he was awarded Fellow of SPIE.